Horizontal Velocity Structure in Waterspouts

R. L. SCHWIESOW

NOAA/ERL/Wave Propagation Laboratory, Boulder, CO 80303

(Manuscript received 12 August 1980, in final form 20 December 1980)

ABSTRACT

We have measured the spatial variation of a single horizontal component of the velocity in a number of waterspouts using an airborne infrared Doppler lidar. In 21 data sets, maximum velocities range from 4.2 to 33.6 m s^{-1} and visible funnel diameters from 6.6 to 90 m. Data were taken at altitudes between 675 m, near cloud base, and 95 m above the surface. The sequences show time development of the velocity as a function of radius at a fixed altitude and the velocity structure at different altitudes and sequential times with a horizontal resolution of ~0.75 m between data points. The variation in velocity structure between waterspouts is large, with some showing marked azimuthal asymmetry and mixing with the ambient flow, and others showing multiple concentric vortex shells.

1. Purpose of study

The objective of the research was to measure some aspects of the spatial variation of velocity in waterspouts. The nature of the instrumentation limited the data to a single horizontal velocity component, which was supplemented by visual and photographic observations. Peak observed velocity was the primary interest, but variation of the tangential velocity with distance from the vortex axis was a secondary interest because it would aid in understanding waterspout dynamics. The intent of this paper is to present a body of observed data and to relate the observations to simple one-dimensional vortex models.

Knowledge of peak velocities and velocity structures in waterspouts aids in understanding the dynamics of small scale (<200 m diameter) atmospheric circulations. The data should be of use in testing tornado models extrapolated to small scale, and the observed structures may suggest appropriate theoretical models for atmospheric vortices. Data on peak winds, vortex diameters, and translational speeds are relevant to calculating wind loads and accelerations on buildings, windborne debris, and harbor facilities.

Direct measurements of waterspout wind, temperature and core pressure have been made by gustprobe instrumented aircraft penetrations and reported by Leverson *et al.* (1977). These authors presented three horizontal velocity structure data runs showing tangential velocities ranging from 5.2 to 28.1 m s^{-1} without yaw acceleration corrections. The life cycle of waterspouts was emphasized by Golden (1974, 1971) in a study of photographic data. Photogrammetrically estimated mean tangential speed was 27 m s^{-1} for one case analyzed. Golden (1974) observed double-walled waterspouts and discussed rotational asymmetries in the spiral band pattern on the sea surface.

Our project was designed to extend previous work by providing greater spatial resolution than the penetration or photogrammetry measurements and by making measurements at an altitude lower than the 400 m reported by Leverson *et al.* (1977). The lidar does not disturb the flow, requires no aerodynamic calibration, and provides more complete velocity spectral information than the other techniques previously applied. Lidar velocity data are objective because no identification and tracking of visible funnel features are required to obtain a velocity estimate, but only one velocity component (along the beam) is measured by the lidar.

2. Measurement and analysis techniques

a. Time and place

Data were collected from 26 August to 14 September 1976 (day 239–258), although the time spent on site and searching covered 16 August to 15 September. This period roughly corresponds to the late-summer peak in frequency of occurrence of waterspouts (Golden, 1973).

The search and measurement area was within a 65 km radius of Key West, Florida. Most spouts were sighted between Big Pine and Marquesas Keys and over the Gulf of Mexico north of the lower Keys.

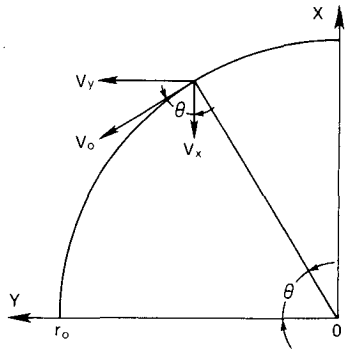

FIG. 1. Velocity component measurement geometry. Doppler lidar measures component V_x of tangential velocity V_0 as a function of coordinate Y along the scan (flight) direction. The radius of the rotating cylindrical shell, here shown in one quadrant, is r_0. The aircraft flight path is parallel to Y with the lidar axis fixed parallel to X.

b. Airborne lidar

Our approach to collecting the desired data involved remote measurement of velocity spectra using an airborne Doppler lidar. A previous paper (Schwiesow *et al.*, 1981) discussed the lidar and interpretation of the velocity spectra. That hardware-oriented study gave details on the instrumentation, spatial averaging along the line of sight, and production of velocity-versus-distance graphs from the time-sequential velocity spectral data. Scanning the vortex was accomplished by the aircraft in straight and unaccelerated level flight with the lidar axis fixed at right angles to the flight path (Schwiesow *et al.*, 1981).

The velocity spectra represent the velocity distributions of all scattering particles in the lidar sensing volume weighted by their backscatter coefficient. Individual velocity measurements are uncertain to ± 0.5 m s^{-1} from component orientation and $\pm 12\%$ from scale-reading uncertainty. Axial distance measurement uncertainty is $\pm 13\%$ from air speed, yaw, and data rate uncertainty. In addition, the overall funnel diameter is uncertain by twice the spatial distance between successive data scans (2 times 0.75 m).

Processed, averaged velocity values from the velocity-versus-distance graphs have less uncertainty than those for individual spectral estimates. On the other hand, low signal-to-noise data scans have larger uncertainty than the base values above for both velocity and distance (see Table 1).

The horizontal velocity component is less than the tangential velocity if the waterspout axis is tipped at an angle ϕ from the vertical in the vertical plane containing the lidar beam. The measured velocity is then $\cos\phi$ times the tangential velocity in the plane perpendicular to the waterspout axis. We have no way of accurately measuring ϕ because this angle does not appear in the photographic data. The measured velocity is then the lower limit of the tangential velocity at the stated radius.

c. Model velocity structure

Consider a rotating cylindrical shell of scatterers with tangential velocity V_0. Fig. 1 indicates the geometry for a lidar measurement. The Doppler lidar measures only the $|V_x|$ component (lidar line of sight along X) as a function of Y from zero to r_0, the radius of the assumed rotating shell. For the quadrant shown, the X-component is $|V_x| = |V_0 \times \cos\theta|$. Angle θ is given through $\cos\theta = |Y/r_0|$, so that the velocity-versus-distance function for the lidar-measured velocity component of a rotating cylindrical shell is

$$|V_x(Y)| = |V_0 Y/r_0| = |\omega Y|, \qquad (1)$$

where Y is the distance from the axis of the cylinder. The angular velocity ω is simply V_0/r_0 for the shell.

The dependence of velocity on distance from the cylindrical axis is graphed in Fig. 2. Note that the sense (sign) of the V_x velocity component is not determined. The graph is linear and extends only to the radius r_0 of the cylinder. For another (almost transparent) scattering cylindrical shell of radius $r_0' < r_0$ rotating at the same angular velocity ω as the outer shell, the graph of velocity versus distance is identical to that for the outer shell out to $Y = r_0'$. A measurement of velocity versus distance cannot distinguish between a single cylindrical scattering shell, a set of nested shells with the same angular velocity, and a solid scattering cylinder rotating at ω.

Existence of more than one lidar-sensed velocity value at a given distance Y requires that more than one angular velocity value be present in the vortex composite. This dynamic difference between concentric rotating elements must follow from velocity value differences no matter what the distribution of backscatter intensity with radius. Backscatter in-

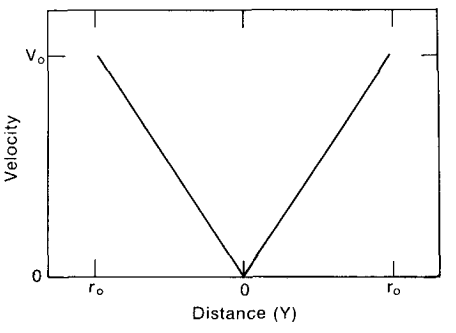

FIG. 2. Ideal dependence of velocity component $|V_x|$ on scan position Y. The velocity structure is identical for both a cylindrical shell and a solid scattering cylinder in uniform rotation. Maximum $|V_x|$ is V_0, the (maximum) tangential velocity of the cylinder.

tensity distribution affects the appearance of the velocity structure plot in detail.

The backscatter intensity from a cylindrical shell changes with distance from the axis. The lidar-path-integrated backscatter is proportional to the chord length of the cylindrical shell because the lidar sampling region is longer than the diameter of any of the waterspouts measured. The chord length is a maximum at the inner diameter of the shell. We would expect an inner shell of radius r_0' to dominate the intensity-weighted velocity spectrum at distance $Y = r_0'$ except that the outer shell attenuates the inner shell return so that inner and outer shell contributions to the velocity spectrum (when both are present) are roughly equal. Fig. 3 illustrates the geometry involved. If the density of scatterers is the same in both shells, the cross-hatched area is greater than the stippled. The difference between the contributions from the cylindrical region near r_0' and regions at larger radii is even larger for a more realistically large (less schematic) ratio of cylinder radius to sample cell diameter.

The consequence of backscatter weighting is that for a uniform distribution of scatterers not in uniform (solid) rotation the lidar return at any distance Y is dominated by the velocity of the cylindrical shell element of radius $r = Y$. The fact that the dominant contribution to the velocity spectrum comes from the region of radius $r = Y$ follows directly from the backscatter weighting geometry of Fig. 3. An idealized spectrum is shown in Fig. 4 where the integrated

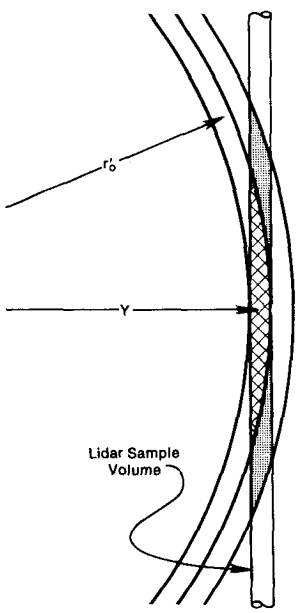

FIG. 3. Geometry showing interaction of sample volume with cylindrical shells. The contribution of the inner shell at r_0' is cross-hatched, and that of the outer shell, stippled. The dominance of the crosshatched region is more striking for a more realistically large ratio of shell radius to sample volume diameter.

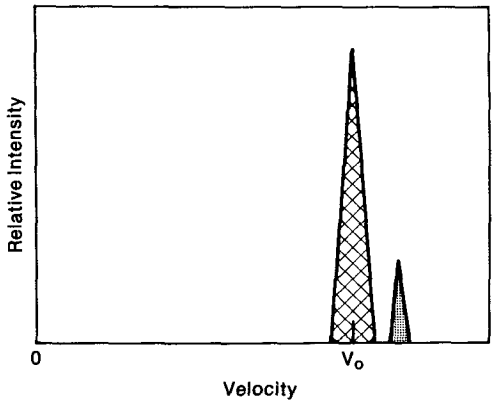

FIG. 4. Idealized velocity spectrum of the $|V_x|$ component for a two-shell model as in Fig. 3. The inner shell is rotating with tangential velocity V_0 and the outer is rotating with a slightly higher velocity. Turbulence would broaden the spectral peaks and merge them.

spectral intensity from the shell r_0' is larger than the contribution from the outer shell. For the sake of illustration, Fig. 4 assumes the angular velocity of the outer shell is larger than that of the inner. Because of the weighting, a graph of velocity versus distance is approximately equivalent to a plot of tangential velocity versus radius.

Turbulence (fluctuations about the mean tangential velocity) in the sample volume will broaden the idealized spectral peaks in Fig. 4 and smooth the spectrum. The other major broadening mechanism is departure from a constant angular velocity. In reality, there cannot be a sudden change of angular velocity as a function of radius as assumed for illustration in Fig. 4; rather, a smooth change of angular velocity results in a broadened spectrum instead of discrete spectral peaks.

If the angular velocity in the vortex is not constant, the mean value (first moment) of the spectrum will be shifted away from the true value $V(Y)$. In other words, if tangential velocity is not a linear function of radius, contributions to the velocity spectrum taken at Y from scatterers not at radius $r = Y$ will have velocities different from $V(Y)$ and will shift the observed spectrum from an ideal one centered at $V(Y)$. The sign of $\partial^2 V_x/\partial r^2$ or of $\partial\omega(r)/\partial r$ determines if the shift is to lower or higher velocities than the actual $V(Y)$. As is obvious from Fig. 4, an increase in angular velocity with radius will shift the spectral mean up from the tangential velocity at $r = Y$, and a decrease will shift it down. In practice, the resolution in Y appears to give narrow enough spectra that spectral shifts from changes in angular velocity with radius are not obvious in the reduced data or in graphs of $V_x(Y)$. An absence of obvious shifts also would result if the scatterers were not well distributed throughout the volume of the vortex but instead were concentrated in a shell at a particular

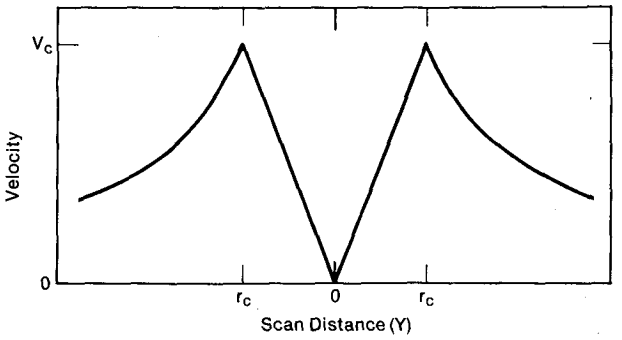

FIG. 5. Idealized plot of the $|V_x|$ component as a function of distance Y scanned from the axis for a Rankine-combined vortex.

radius. However, the possibility of spectral shifts from a variable $\omega(r)$, which would have the effect of making $\omega(r)$ seem more constant than it really is, must be kept in mind in interpreting the observations.

One model for the tangential velocity as a function of radius in an atmospheric vortex is a Rankine-combined vortex, which has solid rotation in the core, where $r < r_c$, and irrotational motion outside the core. The tangential velocity V is then given by

$$V(r) = \begin{cases} V_c r/r_c, & r \leqslant r_c \\ r_c V_c/r, & r \geqslant r_c. \end{cases} \quad (2)$$

Fig. 5 illustrates the expected variation of lidar-detected velocity component V_x with scan position Y for a Rankine-combined model. Actual data, given later, can be compared to the model results in Fig. 5.

Although useful for comparison with experimental data, the Rankine-combined vortex model cannot be a very exact representation. The derivative $V'(r)$ is undefined at $r = r_c$, and the second derivative $V''(r) \to \infty$ at $r = r_c$. This is not physically realistic; actually there must be a smooth transition between the two forms in (2) over a length scale dependent on the vortex type. The transition region may in fact be larger than r_c for some waterspouts. Other departures from the Rankine model are discussed in the results section. The core radius r_c is not necessarily the same as the radius of the visible condensation funnel and generally is less than the spray ring. Golden (1974, 1971) presents the general configuration of waterspouts.

d. Data reduction procedures

Development of the velocity-versus-distance graph as the −3 dB intensity contour of sequential velocity spectra was presented in the lidar-waterspout instrumentation paper (Schwiesow *et al.*, 1981). The width between the contour lines in the velocity dimension is proportional to the range of velocities present in the sensing volume resulting from turbulence and backscatter weighting effects applied to a change in angular velocity with radius. The raw velocity-versus-distance plot is contaminated by relative motion between the aircraft and the vortex axis and by radial inflow to the vortex.

Relative motion between the lidar and vortex along the lidar line of sight adds a constant velocity to the velocity component from rotation. The translation adds to rotation on one side of the axis and subtracts on the other. The effect of translation is to shift the apparent vortex axis (zero line-of-sight velocity component) off the geometric center of the vortex. In contrast to translation, which introduces a velocity effect at all distances Y, the line-of-sight radial inflow component is zero at the edge of the funnel and a maximum at $Y = 0$ on the vortex axis. The lidar data were not detailed enough to separate translation and radial inflow effects, so they were lumped together. In general, translation-inflow velocities at the altitudes where data were taken were a small fraction of rotational velocities, as can be seen from the values in Table 1.

To correct the velocity-distance graphs for translation-inflow, data points on one side of the vortex were reflected about the $V_x = 0$ (distance or abscissa) axis. This procedure removed the artificial sign reversal introduced by lidar homodyne detection. Smooth contour lines were then drawn connecting the data points on either side of the $V_x = 0$ axis, using continuity to clarify contour shape near the vortex axis. The $Y = 0$ axis was apparent from rotational symmetry of the data. Intersection of the $Y = 0$ geometric axis with the contour lines defined a new $V_x' = 0$ abscissa. The contour lines for one side of the vortex were then reflected about the new abscissa to produce a symmetrized velocity-versus-distance graph. A check on the procedure was to note that inner, protected velocity features showed approximately the same velocity on both sides of the axis. The translation-inflow velocity is the difference in velocity between the new and old abscissas.

3. Results

a. Measured data

Table 1 summarizes the reduced waterspout data from the experiment. Waterspouts are identified by the day number and a sequence letter if we obtained useful data on more than one spout in a day. The figure number refers to the velocity structure graph corresponding to that run or the graph similar to the structure for that run if the number is in parentheses.

Maximum observed tangential velocity was 29.6 ± 3.3 m s^{-1}. The peak wind observed (tangential plus translation) was 33.6 ± 3.8 m s^{-1}. This value is similar to that observed in other experiments (Leverson *et al.*, 1977; Golden, 1974). Visible (lidar-de-

TABLE 1. Waterspout data summary.

Number	Figure*	Time (EDT)	Altitude (m) ± 8 m	Maximum velocity component (m s^{-1}) ± (m s^{-1})		Core diameter (m) ± (m)		Diameter (m) ± (m)		Translation (m s^{-1}) ± (m s^{-1})	
239A	(16)	1558:31	615	20.1	2.8	50	14	50	14	—	
239B	6	1600:35	615	8.3	1.1	24	5	24	5	0.5	0.2
	7	1603:30	615	9.6	1.3	24	5	24	5	1.3	0.2
243A	(16)	1417:23	585	9.3	1.6	18	6	18	6	—	
243B	(9)	1421:45	585	4.2	1.1	—		87	16	—	
243C	8	1428:45	585	8.5	1.2	30.5	5	30.5	5	1.1	0.2
243D	(9)	1433:01	520	12.4	1.9	—		90	17	—	
246	(9)	1655:40	125	10.6	1.9	—		71	15	—	
249	(9)	1037:34	125	15.4	2.2	—		82	10	—	
258A	9	1424:58	170	11.5	1.6	8	1	66.3	7.5	0.8	0.2
		1426:17	125	8.2	1.2	6.7	1	—		1.4	0.2
		1430:25	105	12.2	2.0	6	1	—		—	
258B	10	1500:28	675	15.7	1.9	3.7	0.7	17.9	2.5	0.8	0.2
	11	1501:26	675	18.2	2.1	4.5	0.7	14.9	2.5	0.3	0.1
	12	1502:45	675	18.2	2.1	4.5	0.7	14.5	2.5	0.3	0.1
258C	13	1505:24	160	21.7	2.5	6.6	1.5	6.6	1.5	0.8	0.2
	14	1508:51	95	14.3	2.2	14.2	1.6	55.1	6.5	1.1	0.2
258D	15	1518:40	615	25.2	2.8	27.6	3.5	27.6	3.5	6.7	0.9
	16	1520:46	460	29.6	3.3	14.9	2.5	14.9	2.5	4.0	0.5
	17	1524:08	160	25.9	3.0	4.9	0.7	23.8	3.5	0.6	0.2
	(17)	1525:20	105	13.8	2.1	—		28.3	7	—	

* Parentheses mean that the structure of the spout was similar to the figure indicated.

tected) vortex diameters ranged from 90 ± 17 m to 6.6 ± 1.5 m. Data were taken at altitudes ranging from 95 m to near cloudbase at 675 m.

b. Dynamic structure

The visible funnel of many waterspouts was not in solid, constant-angular-velocity rotation. Comparison of solid rotation in Fig. 2 with waterspout velocity structure graphs for waterspouts 239B (Figs. 6 and 7), 258B (Figs. 10 and 11), and 258D (Fig. 17) shows that some waterspouts contained cylindrical shells rotating at different angular velocities. Although the homodyne lidar does not determine the sense of rotation, it is reasonable to assume that all elements were rotating in the same direction since the very high velocity shears resulting from opposite rotations are improbable.

Golden (1974) hypothesized that the outer funnel in a double-walled waterspout resulted from locally enhanced moisture content and intensification of the vortex. The lidar results show that there is a dynamic difference between inner and outer funnels. All observed multiple-velocity waterspouts (those with multiple peaks in the velocity spectra) were composed of concentric elements because the spectral peaks persisted from spectral scan to spectral scan. This behavior is in contrast to the subvortices observed in dust devils (Schwiesow and Cupp, 1976),

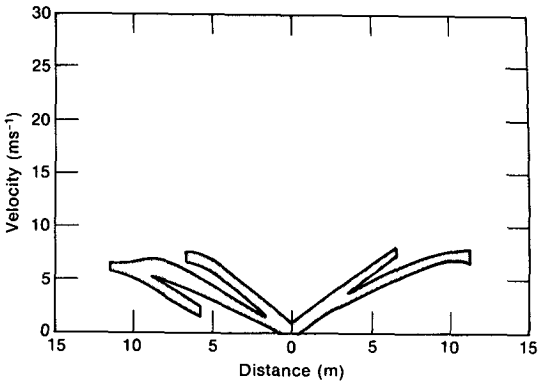

FIG. 6. Velocity structure for waterspout 239B at an altitude of 615 m. Note that the inner core was at a higher angular speed than the outer wall. The structure on the upwind side of the vortex (left in the figure) differed from that of the lee side (right), showing interaction with ambient flow. Mixing with more slowly rotating air reduced the tangential velocity compared with that of the lee side and increased turbulence. A slowly rotating outer shell existed only on the windward side. Translation-inflow was 0.5 m s^{-1}.

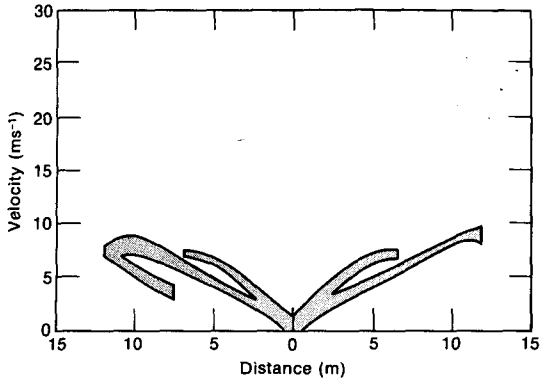

FIG. 7. Vortex 239B at 615 m altitude ~ 3 min later than in Fig. 6. The outer wall speeded up and more closely approximated the solid rotation shown in Fig. 2. The inner core slowed down at the outer edges, departing from solid rotation. Translation-inflow increased to 1.3 m s^{-1}.

which are not concentric with the main vortex and do not persist because they move through the sample volume faster than the axis of the main vortex does. Unequal waterspout pairs with oppositely directed tilt, somewhat similar to dust devil subvortices, have been observed before (Golden, 1970) and were observed twice during this experiment. The large length-to-diameter ratio of the spouts and their coaxial structure are similar to rope-type dust devils rather than to the broader, more turbulent vase-type devils, which have subvortices imbedded in the wall of the parent vortex. The decay mode of the waterspouts, a snaking of the thin vortex tube (Golden, 1974), is similar to the decay of rope-type devils rather than to that of vase-type devils, which decay with a turbulent energy cascade to smaller scales.

In spout 239B there were two distinct cylindrical shells and a minor outside shell that was marked by weak condensation only on the windward side of the vortex. In Fig. 6 the inner element is close to solid rotation while the outer shell shows some decrease in angular velocity toward the outer edge of the funnel. There was enough condensation in vortex 258B (Figs. 10 and 11) to mark the transition region between inner and outer funnels. Except for the transition region, the waterspout showed two distinct values of rotation out to a radius of 6 m. When a spray ring existed, as in 258D (Fig. 17), the structure was more complex and included three elements in this case, for example. In every case the inner vortex showed the higher angular velocity.

Outside the radius of maximum velocity the tangential velocity generally decreased with increasing radius, but the data do not prove an r^{-1} dependence. Leverson *et al.* (1977) found a similar departure from r^{-1}, which they suggested might be due in part to instrumental effects. Departures from r^{-1} may also be due to inflow, which is assumed zero in the Rankine-combined model. For the distances from the axis observed in this experiment the tangential velocity approached a locally constant value different from zero (Figs. 9, 10, 14, and 17), although the rotation must approach zero far enough from the spout.

Most of the velocity structure graphs show a smooth transition between solid rotation and r^{-1} parts of the velocity dependence, as in Figs. 8 and 12 for example. Note that the edge of the condensation funnel sometimes corresponded to the velocity peak (e.g., Figs. 13, 16, and 18) but sometimes did not (e.g., Figs. 8, 10, 12, 17, and 19). The radius of maximum optical density can be at the edge of the funnel, as in Fig. 18, or inside the limits of funnel condensation, as in Fig. 19. Kangieser (1954) discussed the hollow structure of waterspout tubes assuming a Rankine-combined model for the angular velocity. With this model, he deduced a radius dependent convergence to explain a structure with two concentric shells. Departures from the velocity distribution of the Rankine-combined model, as measured by the lidar, introduce an additional degree of freedom into the analysis. In any event, where the visible waterspout funnel is dominated by condensation rather than spray, the distribution of backscatter intensity is closer to a cylindrical shell than to a solid cylinder of uniform backscatter distribution in the volume. Sufficient flow markers exist inside the shell to reveal departures from solid rotation as shown in the curvature of the velocity structure graphs in Figs. 6 and 7, for example.

Double-wall structure was especially apparent when the condensation funnel extended to less than 50% of the distance from cloud to surface, because the inner funnel was always somewhat longer than the outer. A clear cue of double-wall structure is the characteristic three-pointed funnel termination visible even on a two-dimensional image.

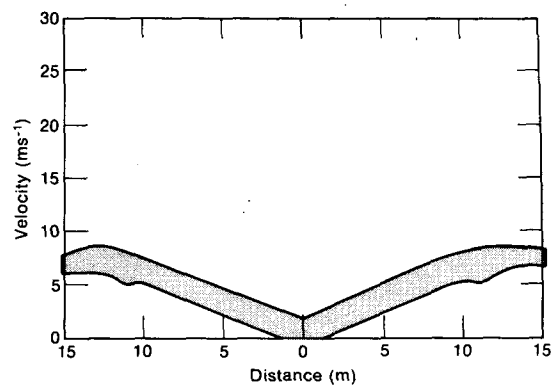

FIG. 8. Velocity structure for waterspout 243C at 585 m altitude showing a slight slowdown from ambient mixing on the windward (right) side. Note a shell of increased turbulence approximately ¼ radius in from the outer limits of condensation. Translation-inflow was 1.1 m s^{-1}.

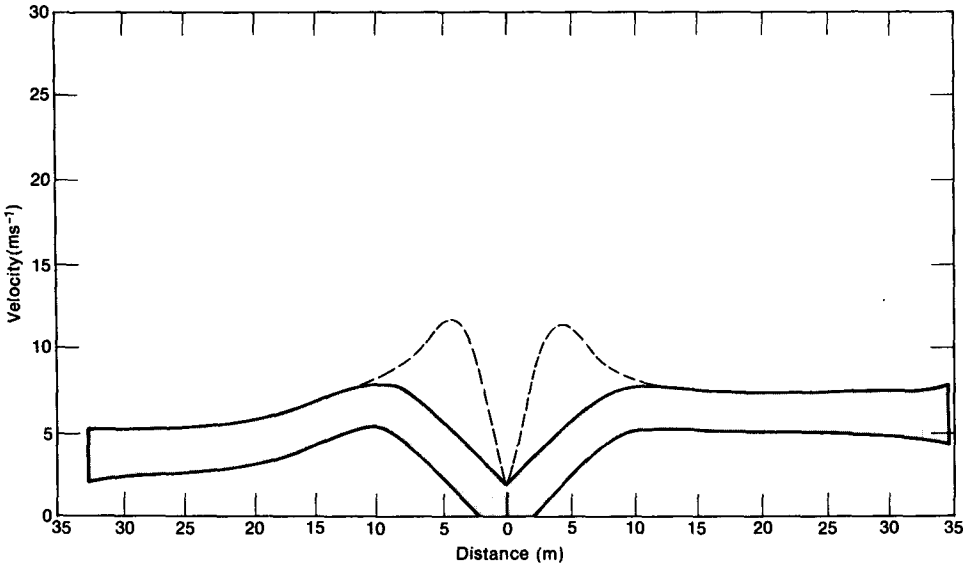

FIG. 9. Velocity structure for spray ring 258A taken at 170 m above the surface. The central core is shown dashed because the intensity was more than 3 dB below the low-velocity portion of the spectrum, but definitely visible. Note significant departure from solid rotation in the spray ring beyond 8 m radius and the rotational asymmetry (right and left differences) at large radii. Translation-inflow was 0.8 m s^{-1}.

c. Asymmetry

The visual appearance of a waterspout's environment does not exhibit rotational symmetry (Golden, 1974). As expected, the velocity structure was also asymmetric in many cases. Asymmetry results from inflow to the vortex and from mixing with slowly rotating ambient air moving past the waterspout. A symmetric velocity structure graph means either that the visible (condensation) funnel was symmetric or that the asymmetric parts of the waterspout were near the lidar line of sight through the vortex axis and therefore not detected as line-of-sight components.

Waterspout 239B illustrates both dynamic and backscatter asymmetry with the ambient flow flowing past the spout from left to right in Fig. 6. The cool, moist storm outflow moving by the waterspout supported enough condensation to make the entrained, rotating air show up as a low-velocity shield on the

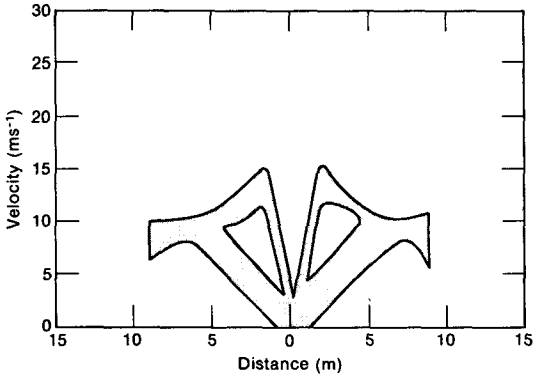

FIG. 10. Velocity structure for waterspout 258B at an altitude of 675 m. This is a double-walled funnel with sufficient condensation to mark the flow between and outside the two major shells. Elements included an inner core, an outer shell, a transition region of decreasing velocity with increasing radius connecting the inner core and outer shell, a constant-velocity region outside the outer constant angular velocity shell, and turbulent interaction with the ambient flow at the edges of the condensation funnel. Note the similarity of double-wall structure to those in Figs. 6 and 7. Translation-inflow was 0.8 m s^{-1}.

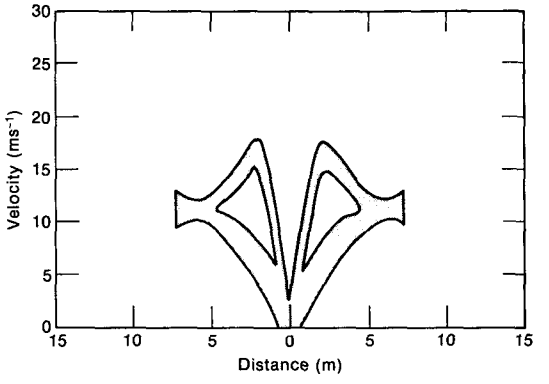

FIG. 11. Double-walled vortex 258B 1 min later than in Fig. 10. The inner core had increased in velocity and widened while the outer constant-velocity part of the funnel had contracted and turbulent interaction with the environment had decreased. Mixing between the inner and outer vortex elements introduced a slight departure from constant angular velocity with radius in the outer shell. A reduction in translation-inflow to 0.3 m s^{-1} indicates reduced movement, reduced inflow, or both.

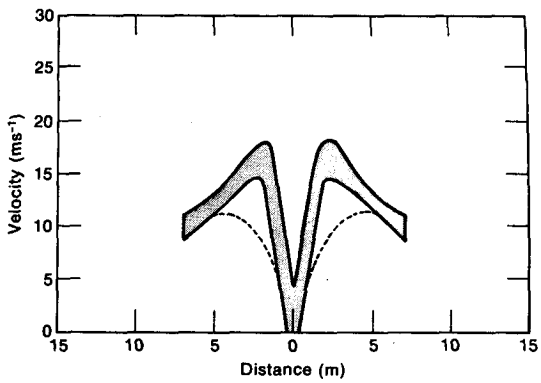

FIG. 12. Vortex 258B slightly more than 1 min later than in Fig. 11. The inner core dominated the circulation, although indications of the old outer shell persisted with a backscatter intensity more than 3 dB below the peak backscatter from the stronger main core. The condensation funnel had again contracted slightly overall, and the velocity at the outer edges was slightly less. The double-wall structure had disappeared. Translation-inflow was 0.3 m s^{-1}.

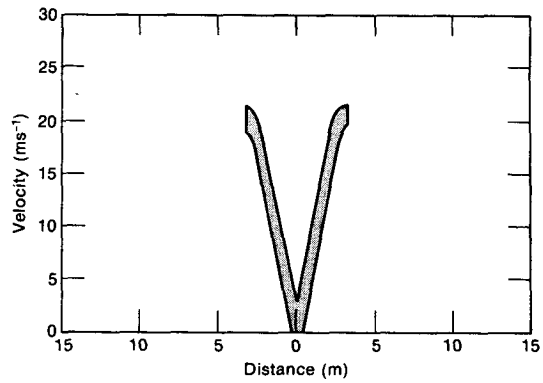

FIG. 13. Waterspout 258C at 160 m above the surface. The simple, small-diameter, high-rotational-speed velocity structure shows almost pure solid rotation. At the edges of the condensation funnel, departure from solid rotation gave smooth transition to lower angular velocity flow outside the visible (lidar-measured) portion of the waterspout. Translation-inflow was 0.8 m s^{-1}.

windward (left) side of the spout. As the entrained air moved approximately half way around the funnel toward the lidar, the condensation evaporated, leaving no lidar-detectable tracers. The mixing of ambient air into the rotating funnel slowed tangential velocity on the upwind side of the waterspout by ~3 m s^{-1} compared to that of the lee side. Increased turbulence (width between −3 dB contour lines) was associated with the mixing process; compare left and right branches of the velocity structure graph. The inflow and mixing effect of slowing tangential velocity extended to the inner vortex of the double-vortex system of Fig. 6 as well. Three minutes later, as shown in Fig. 7, the mixing effects on tangential velocity still existed, but the mixing did not extend as deeply into the vortex, having little or no effect on the inner funnel, for example. The region of maximum turbulence also moved to larger radius between the times of Figs. 6 and 7.

The strongest asymmetry of the cases graphed was waterspout 258D, Fig. 15. Near cloudbase, the inflow-translation was 6.7 m s^{-1} with a peak tangen-

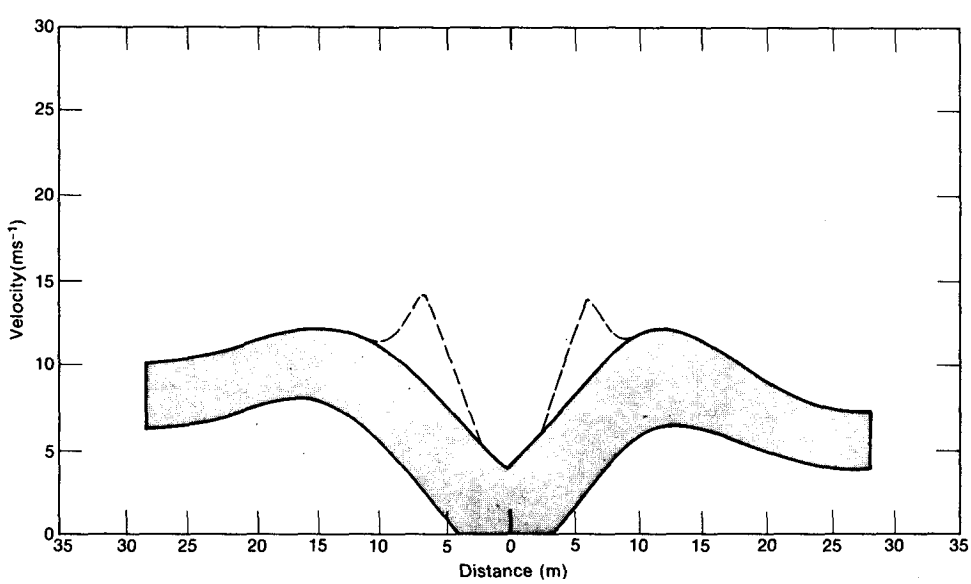

FIG. 14. Spray ring associated with vortex 258C at 95 m altitude, 3.5 min after the view shown in Fig. 13. The inner core, with an intensity more than 3 dB below that of the spray ring backscatter, was lower in speed than at 160 m altitude. The spray ring shows solid rotation out to ~10 m radius and a transition to decreasing tangential speed with increasing radius beyond. Note right-left asymmetry similar to that in Fig. 9. Translation-inflow was 1.1 m s^{-1} at this level.

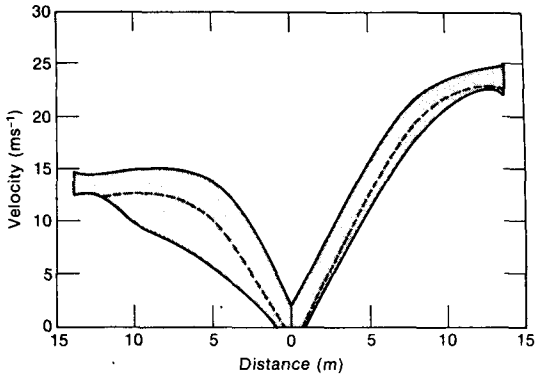

FIG. 15. Waterspout 258D at 615 m altitude, near cloud base. Striking asymmetry was associated with a large translation-in/outflow of 6.7 m s^{-1}. Mixing with slowly rotating ambient air reduced the tangential velocity and increased the turbulence on windward (left) side of vortex, as in Fig. 6. The velocity structure between the dashed line and the upper velocity contour represents the symmetric part of the individual velocity spectra; below the dashed line is the lower-intensity spectral tail related to turbulence.

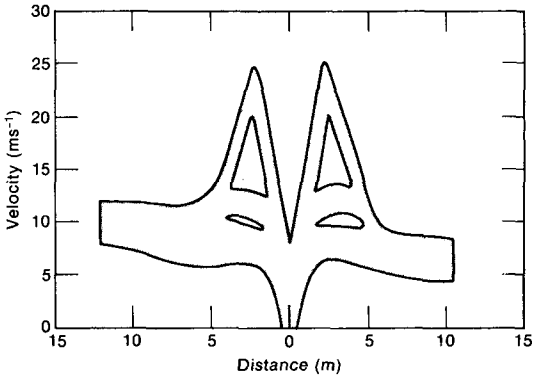

FIG. 17. Waterspout 258D at the top of the spray ring (160 m) 3 min after the view shown in Fig. 16. The inner core was further contracted and showed a transition region to the spray sheath flow similar to that in Figs. 10–12. An intermediate outer vortex shell existed between the inner core and the spray ring. The spray ring showed asymmetry for radii > 5 m, similar to that shown in Figs. 9 and 14, even though this ring was of much smaller outer diameter. Translation-inflow was 0.6 m s^{-1}, which is smaller than the values for the same vortex earlier and higher up.

tial velocity of 25.2 m s^{-1} and a tangential velocity deficit or asymmetry between advancing and retreating sides of the vortex of ~9.5 m s^{-1}. This large asymmetry was associated with a much larger turbulence value on the upwind side of the vortex than on the lee side. Note that the asymmetric flow in this case existed for a spout with otherwise simple velocity structure. A large translation-inflow velocity component does not necessarily imply large asymmetry, as illustrated in Fig. 16 for the same waterspout at a lower level and slightly later time.

Spray sheaths on waterspouts measured at altitudes below 180 m exhibited asymmetry at large radii for all the three cases graphed. In Figs. 9, 14 and 17 the spray rings are symmetric at least out to the radius of inner funnel peak velocity but become asymmetric farther out. The asymmetries take the form of asymptotic approach to different tangential velocity values on each side of the waterspout, even after near-axis translation-inflow velocities are cor-

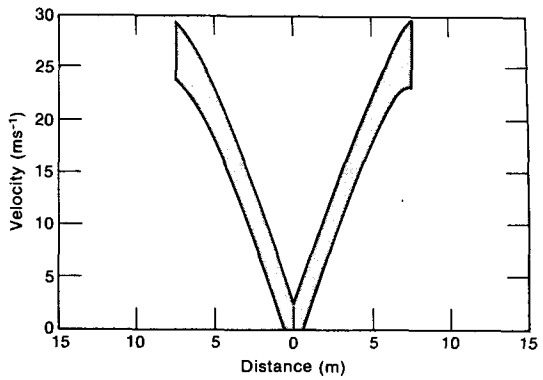

FIG. 16. Waterspout 258D at midlevel (460 m) 2 min after the view shown in Fig. 15. The simple, nearly solid-rotation velocity structure shows the highest tangential velocity observed in the experiment and the usual transition to reduced angular velocity near the edge of the condensation funnel. The funnel (core) diameter was approximately half that near cloudbase. Translation-inflow was 4 m s^{-1}.

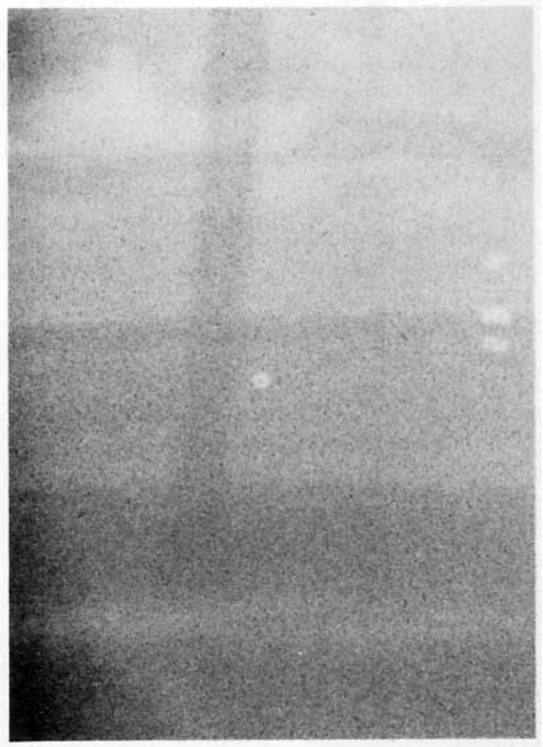

FIG. 18. Simple, single-walled waterspout of moderate optical density characteristic of the type of spout represented by 258C (Fig. 13).

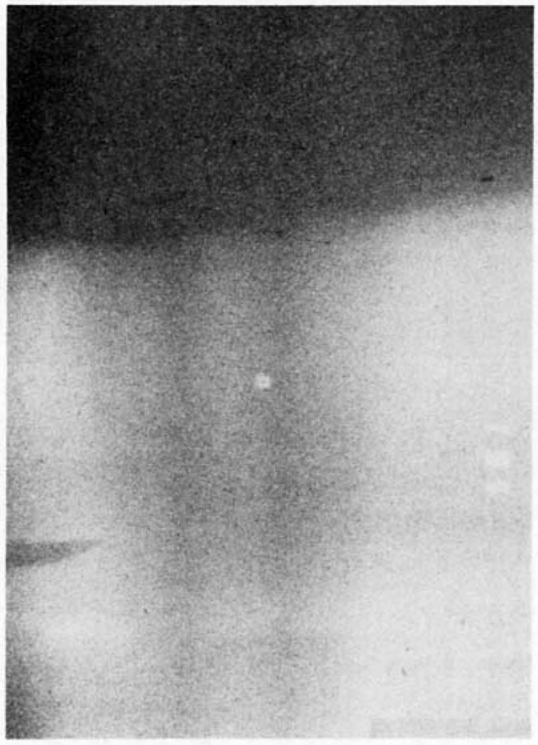

FIG. 19. Single-walled waterspout with turbulent region, marked by condensation, outside of the visual core. This pattern is characteristic of the velocity structures represented by waterspout 258B in the single-wall stage (Fig. 12).

rected for. Large-radii velocity differences were 2.5–3.5 m s^{-1} for these cases, which were at least three times the corresponding translation-inflow values. Such departures from symmetry are reasonable in light of the asymmetric spiral inflow bands visible on the water surface (Golden, 1974).

In the spray sheath or spray collar, radial velocities are present and are likely to be both inflow and outflow. The outflow consists of large spray drops centrifuged out, while smaller droplets follow the presumed inflow convergence. The fact that the lidar reads this mixed particle flow as inflow (the same as higher in the waterspout) means that the small cloud droplets sufficiently outnumber the larger drops to give a backscatter intensity dominated by smaller droplets.

d. Changes with time

Time sequence data at a constant height were taken for waterspouts 239B and 258B. In both cases the spouts were in the increasing velocity rather than decay stage.

In the 3 min between the times of Figs. 6 and 7 for 239B the vortex became more independent of outside influences. The outer shell increased in velocity near the outer edge of the funnel, more closely approaching a solid rotation model. The maximum turbulence region on the windward side moved out, and ambient air mixing effects did not reach as deeply into the vortex. The internal dynamics of the concentric two-shell funnel showed the result of interaction between the elements as slowing at the outer edges of the more rapidly rotating inner funnel. This interaction caused a departure of the inner core from the solid rotation model.

Waterspout 258B was also a double-walled vortex. Comparison of Figs. 10 and 11 shows that in 1 min the spout increased in velocity and decreased in overall diameter, although the inner core expanded slightly. During the next 1.5 min the peak velocity and diameter remained approximately unchanged, but the two-shell velocity structure changed. The outer shell essentially disappeared and was mixed into the higher-velocity inner core, which then dominated the velocity structure. The linear, solid-rotation character of the outer shell in Fig. 10 departs from solid rotation in Fig. 11, showing the first stages of mixing between the shells and eventual control of the velocity structure by the inner vortex. This internal energy rearrangement is in contrast to 239B, where the outer shell started to dominate. In the single-vortex stage, waterspout 258B appeared to follow qualitatively a symmetric, smoothed, Rankine-combined vortex model as far as the condensation funnel extended. Note how the transition region between the inner and outer shells in Fig. 10 (absent in 239B) becomes the r^{-1} irrotational flow region in Fig. 12.

The changes in velocity structure with time during the growth phase generally included an increase in angular velocity, a slight decrease in diameter, and mixing interaction between dynamically different vortex elements. Golden (1974) also noticed the gradual disappearance of the visual double structure with time for a double-walled spout.

e. Height differences

Because of the time required to change altitude, data passes at different heights also included time changes. Some aspects of height differences persisted with time. Velocity structure differences between the spout above the spray sheath (Fig. 13) and below (Fig. 14) show the much larger diameter of the spray sheath and symmetric (above spray) versus asymmetric (below) flows. Typically the core diameter increased with height, while the vortex picked up additional larger-diameter scattering shells at low altitude. The continuation of the 6.6 m diameter funnel in Fig. 13 at 160 m altitude to smaller diameter at 95 m altitude was probably obscured by the spray sheath and the 14.2 m shell, which was itself more than 3 dB below the spray scattering radiance.

Waterspout 258D was unusual because the con-

densation funnel extended completely from cloud to surface, allowing a data pass at 460 m altitude between cloudbase and spray sheath. Tangential velocity was a maximum of 29.6 m s^{-1} at midlevels and was slightly less near cloud base (25.2 m s^{-1}) and in the spray sheath (25.9 m s^{-1}). The velocity decrease between 460 m and 160 m altitude was probably real because it contrasted with usual time changes; the increase in tangential velocity between 615 and 460 m may have been partly due to an overall velocity increase with time. Near cloudbase the core diameter increased with height as shown in Table 1. The spray sheath extended to 160 m altitude and increased in diameter closer to the surface. This size dependence is consistent with earlier photographic data (Golden, 1974).

In general, the tangential velocity at the peak velocity radius did not change greatly with altitude. It tended to be a maximum at midlevels where symmetry observations showed less interaction with the environment than near cloud base and near the surface. The condensation funnel diameter increased with altitude while the larger diameter spray sheath or low-level outer shell decreased in diameter with height until it ceased to exist between 100 and 200 m, depending on the particular circumstances.

f. Qualitative observations

Although the lidar did not measure vertical velocity, evidence for values larger than the horizontal tangential velocity was observed visually. For example on spout 258D at 1520:40 an upward helix at 60° ± 10° pitch angle from the horizontal was noted near 460 m altitude. This vortex was a large, energetic, cyclonic waterspout with a condensation funnel from cloud to surface. By 1525:28 the helix pitch in the vicinity of 100 m above the surface had turned downward at ~45°, which emphasizes the changes in velocity structure of a waterspout with time.

Although most of the data were taken when at least a partial funnel was visible, vortex 246 was in the early stages of development. The only visual indication of the vortex was a surface spiral pattern. This is stage 2 of Golden's (1974) waterspout life-cycle analysis. The circulation pattern was large enough and the aerosol backscatter strong enough that a weak lidar signal existed. We observed a maximum velocity of 10.6 ± 1.9 m s^{-1} for this example (see Table 1) at an altitude of 125 m. There is no other spiral pattern velocity data with which this value may be compared.

Occasionally, we took data on diffuse funnel clouds that showed no tangential velocity on the Doppler spectra. We conclude that significant rotation can cease in some cases before the cloud droplets in the funnel completely evaporate.

Both cyclonic and anticyclonic vortexes were observed. Larger spouts tended to be cyclonic during this experiment, but the existence of both directions of rotation means that waterspout circulation cannot be completely controlled by synoptic-scale circulation.

Observations on conditions favoring waterspout development based on searching for data from 15 August to 15 September 1975 (land-based) and from 15 August to 15 September 1976 (aircraft-based) may help others engaged in future waterspout experiments. These qualitative views are supplemental to quantitative, large-scale statistics (Golden, 1973). The largest, longest lasting, and most energetic spouts were associated with large thunderstorm groups that produced heavy rain and lightning during the time of the waterspout, but were spatially separated from it. The parent convective systems often lasted over 30 min. Most spouts occurred on the leading edge of the cold outflow toward the front of the storm. This is consistent with the two-dimensional storm model of Ludlam (1961), which is applicable to the summer Florida Keys where vertical shears are not strong and veering of the wind with height is not pronounced enough to make a three-dimensional model necessary. There seemed to be no consistent relationship between the various operational forecasting stability indexes and those thunderstorm days on which spouts occurred.

Large storms are not required for waterspout formation. A few spouts formed from convective cells that never did produce rain. A few others formed from weak convective lines. The existence of a rain shaft did not preclude spout observations.

Extremely low surface winds (<1.5 m s^{-1}) were not conducive to waterspout observations in our experience. The largest spouts and most numerous sightings appeared to be downwind of land masses by 15 to 30 km. These two observations lead to the hypothesis that mesoscale vorticity generated by flow past the relatively isolated Keys is a major source of circulation and horizontal shear that is subsequently concentrated by updraft stretching to produce waterspouts. The situation is analogous to von Kármán vortex trails observed in the lee of isolated islands on some satellite imagery. Although the hypothesis is not proved by our observations, it serves as a working guide for spout searching when the wind at a particular time is known.

The correlation between location of spout sightings and the wind direction at the time of sighting has not yet been quantitatively investigated; previous statistics concern average sighting azimuth and average wind direction during any sighting. The most spectacular spout-observing day of our experiment was on 14 September 1976, when eight spouts were spotted in 1 h on the west side of a large storm located ~20 km WNW of Big Pine Key in a generally ESE flow. Six other spouts were spotted NW

from Key West, associated with another storm, and estimated to be approximately 15 km downwind (WNW) of Sugarloaf Key at approximately the same time as the aircraft observations. Both of these sighting groups are consistent with the hypothesis. Local Key West observers consider the Marquesas area, 15–20 km downwind of Key West for prevailing easterly winds, to be a "hot spot" of waterspout activity.

4. Conclusions

Waterspouts occur with a wide variety of velocity structures and radial aerosol density distributions. In all cases observed the appearance and structure of the waterspouts were concentric, with more or less asymmetry introduced by inflow and translation effects.

One of the most significant departures of waterspouts from the Rankine-combined vortex model was the existence of cylindrical shells with different rates of angular rotation for the different vortex elements in some waterspouts. The spouts exhibited a smooth transition between solid rotation (tangential velocity proportional to radius r from the vortex axis) and approximately irrotational motion (tangential velocity approximately proportional to r^{-1}). The radius of the visible funnel did not necessarily correspond to the radius of maximum tangential velocity even at heights well above the spray sheath.

The maximum tangential velocity observed was 29.6 ± 3.3 m s^{-1} at midlevel (460 m) for a large, fully developed waterspout having a diameter of 14.9 ± 2.5 m at that altitude. The peak wind observed (tangential plus translation) was 33.6 ± 3.8 m s^{-1}. Measured diameters were as large as 90 ± 17 m near cloudbase and 82 ± 10 m for a spray sheath at 125 m altitude. The smallest spout measured had an infrared scattering diameter of 6.6 ± 1.5 m at 160 m height just above a spray sheath of 55.1 ± 6.5 m diameter at 95 m altitude.

Future Doppler lidar velocity measurements of waterspouts and other atmospheric vortices would add much to our knowledge if they would include data on the vertical velocity component and on the tangential-to-radial velocity component ratio both at the edge of the funnel and on axis. Obtaining these data requires much instrumentation development. Flying a box pattern around the waterspout (probably with 270° turns at the corners) rather than single passes would provide additional information on asymmetry of the flow, especially in the spray ring area. Data at altitudes from ~2–100 m above the surface, in the primary inflow region for the waterspout, would require a different aircraft platform for the lidar. A seaplane should provide necessary safety at very low levels and required mobility for waterspout intercept.

Acknowledgments. R. E. Cupp and P. C. Sinclair were important members of the data-gathering team. M. J. Post helped with data digitization. R. Urbanak, meteorologist in charge, and the staff of the NWS office at Key West provided meteorological support and facilities for the field experiment. This work was supported in part by the U.S. Nuclear Regulatory Commission under Agreement RES-76-106 NRC FIN, with guidance from R. F. Abbey, Jr.

REFERENCES

Golden, J. H., 1970: The lower Florida Keys waterspout project, May–September 1969. *Bull. Amer. Meteor. Soc.*, **51,** 235–236.

——, 1971: Waterspouts and tornadoes over South Florida. *Mon. Wea. Rev.*, **99,** 146–154.

——, 1973: Some statistical aspects of waterspout formation. *Weatherwise*, **26,** 108–117.

——, 1974: The life cycle of Florida Keys' waterspouts I. *J. Appl. Meteor.*, **13,** 678–692.

Kangieser, P. C., 1954: A physical explanation of the hollow structure of waterspout tubes. *Mon. Wea. Rev.*, **82,** 147–152.

Leverson, V. H., P. C. Sinclair and J. H. Golden, 1977: Waterspout wind, temperature and pressure structure deduced from aircraft measurements. *Mon. Wea. Rev.*, **105,** 725–733.

Ludlam, F. H., 1961: The hailstorm. *Weather*, **16,** 152–162.

Schwiesow, R. L., and R. E. Cupp, 1976: Remote Doppler velocity measurements of atmospheric dust devil vortices. *Appl. Opt.*, **15,** 1–2.

——, ——, P. C. Sinclair and R. F. Abbey, Jr., 1981: Waterspout velocity measurements by airborne Doppler lidar. *J. Appl. Meteor.*, **20,** 341–348.